



Full length article

Following dislocation patterning during fatigue



A. Irastorza-Landa ^{a, b}, H. Van Swygenhoven ^{a, b, *}, S. Van Petegem ^a, N. Grilli ^{b, c},
A. Bollhalder ^d, S. Brandstetter ^e, D. Grolimund ^a

^a Swiss Light Source (SLS), Paul Scherrer Institut, CH-5232 Villigen PSI, Switzerland

^b NXMM Laboratory, IMX, École Polytechnique Fédérale Lausanne (EPFL), CH-1015 Lausanne, Switzerland

^c Laboratory for Nuclear Materials (LNM), NES, Paul Scherrer Institut, CH-5232 Villigen PSI, Switzerland

^d Laboratory for Developments and Methods (LDM), NUM, Paul Scherrer Institut, CH-5232 Villigen PSI, Switzerland

^e DECTRIS Ltd., Täferweg 1, CH-5405 Baden-Dättwil, Switzerland

ARTICLE INFO

Article history:

Received 12 February 2016

Received in revised form

1 April 2016

Accepted 5 April 2016

Available online 19 April 2016

Keywords:

Dislocation

Pattern formation

Fatigue

X-ray diffraction

ABSTRACT

Precursors of failure are dislocation mechanisms at the nanoscale and dislocation organization at the mesoscale responsible for long-range internal stresses and lattice rotation. Detailed information on the link between both scales is missing, computationally and experimentally. Here we present a method based on x-ray Laue diffraction scanning providing time and sub-micron spatially resolved evolution of geometrical necessary dislocations in volumes that are similar to what advanced computational models can achieve. The approach is used to follow dislocation patterning during accumulation of fatigue cycles using a newly developed miniaturized shear device. Performed on Cu during cyclic shear, it reveals early dislocation patterning influenced by pre-existing dislocation structures. The quantitative information on non-homogeneous structure formation and its evolution corresponds to the need for synergies with continuum dislocation plasticity simulations of fatigue or any other type of plastic deformation.

© 2016 Acta Materialia Inc. Published by Elsevier Ltd. This is an open access article under the CC BY-NC-ND license (<http://creativecommons.org/licenses/by-nc-nd/4.0/>).

1. Introduction

Plastic deformation in metals results from the motion of interacting dislocations developing heterogeneous structures with dislocation depleted and dislocation rich zones [1,2]. Advanced x-ray diffraction techniques have demonstrated a broad distribution of elastic strains within the dislocation depleted zones [3] and confirmed that these regions show intermittent dynamics and transient behaviour during loading [4]. While failure occurs at the macroscale, the pattern has a typical lengthscale at the micron scale and its formation involves multiple dislocation interactions and slip mechanisms at the nanometer scale. That is why the transition from homogeneous to heterogeneous dislocation microstructures is difficult to describe [5,6]. Computational models at all length-scales have been used to understand particular aspects of dislocation patterning [7–11]. However, to capture fully the transition from uniform to non-uniform dislocation microstructures discrete dislocation models or density based dislocation dynamics models are required [9–15], and of equal importance, experimental

methods must be available to validate the models.

In those computational models, dislocations are often separated into two different categories: statistically-stored dislocations (SSD), which evolve from random trapping processes during plastic deformation and geometrically-necessary dislocations (GND) [16]. The concept of GND was already introduced by Nye [17] to rationalize the compatibility of elastic-plastic deformation in materials experiencing strain gradients. GNDs introduce a characteristic length scale in the continuum formation of plastic deformation and give rise to deformation-induced long-range internal stresses [5,18]. The distribution of GND density can be calculated from experimental measurements of local crystallographic misorientation.

Electron channelling contrast imaging can spatially resolve dislocation patterns over several tens of micrometres close to the surface [19]. This technique however cannot distinguish between GND and SSD. GND density distributions in a 20 nm surface layer can be separately obtained by electron backscattering (EBSD) [20] with a nm spatial resolution. When combining EBSD with a serial sectioning, information on GNDs can be extended to the third dimension [21]. X-ray diffraction can resolve three-dimensionally (3D) and non-destructively local lattice rotation and elastic strain fields with a spatial resolution of the order of a micron depending

* Corresponding author.

E-mail address: helena.vanswygenhoven@psi.ch (H. Van Swygenhoven).

on the beam diameter [22–26]. The technique is however slow [27]. Performed on thin sections of a deformed crystal it provided the probability density distribution of local misorientation [25].

The above-mentioned methods provide detailed information about the microstructure after a certain amount of strain, but they cannot teach us how patterning forms and evolves. To increase synergism with dislocation density based computational schemes, we designed an approach based on 2D Laue diffraction scans. As dislocation densities are integrated over the sample's thickness along beam direction, a template-matching technique is used for statistical information on the orientation spread in the beam direction. The method is applied during cyclic reversed shear at intermediate strain amplitudes on a Cu single crystal oriented for single slip. In this configuration, it is expected to form the so-called channel-vein structure before the gradual transformation into persistent slip bands [28]. Veins consist of an agglomeration of edge dipoles, surrounded by GNDs. Channels on the other hand are regions with very low SSD and no GNDs. A few phenomenological models have been put forward to explain this particular pattern [1,5,29], but there is no general understanding on the formation and evolution.

2. Experimental method

2.1. Shear device

A dedicated miniaturized deformation rig was built to apply reversible shear. A schematic view of the machine is presented in Fig. 1. The rig has dimensions of $200 \times 900 \times 150 \text{ mm}^3$. The frame is made of an AlMgSi alloy. On the back side an opening of 100° is

created for a large angular acceptance. Reversible shear is induced by two pins that sequentially push on either side of the sample. The pins are mounted on two Smaract linear actuators (SLC-1760) with 7N blocking force, sub-nanometer scan resolution and 41 mm travel range. Two 5N load cells (Transducer Techniques, USA) measure the applied force on the pins. In order to compensate gravity a counterweight is installed for the lower linear actuator. On the top side of the specimen a cantilever is installed in between pin and sample. This system measures the actual displacement of the upper pin with a Renishaw Tonic optical encoder with 20 nm resolution.

The shear device is controlled with in-house written LabVIEW routines. During the complete test both pins remain into contact with the sample. When one pin pushes on the sample the second pin retracts. A PID-control loop ensures that the force on this second pin remains zero.

2.2. Sample preparation and orientation

The samples are machined from $19 \times 19 \times 2 \text{ mm}^3$ copper single crystals with 99.999% purity, purchased from Mateck GmbH, Germany. First bores and grooves are machined. Then the samples are annealed at 800° for 2 h with long cooling time, mounted on the sample holder and finally machined by electric discharge machining to a Miyauchi's geometry [30] as shown in Fig. 2a. It consists of two external immobile parts fixed with screws and a central moving area displaced with the pins from the shear rig. These parts are separated by channels and by two symmetric milled $150 \mu\text{m}$ thick grooves, corresponding to the shear zones. These shear zones are furthermore locally thinned by picosecond pulsed

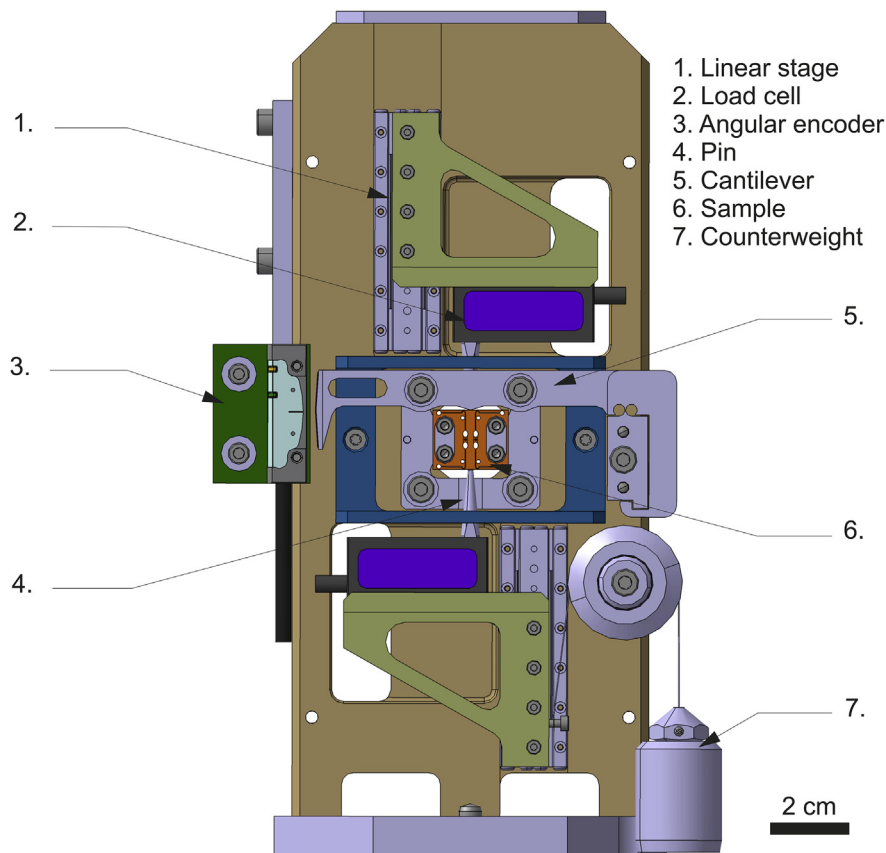


Fig. 1. Schematic view of the deformation rig that allows applying reversible shear.

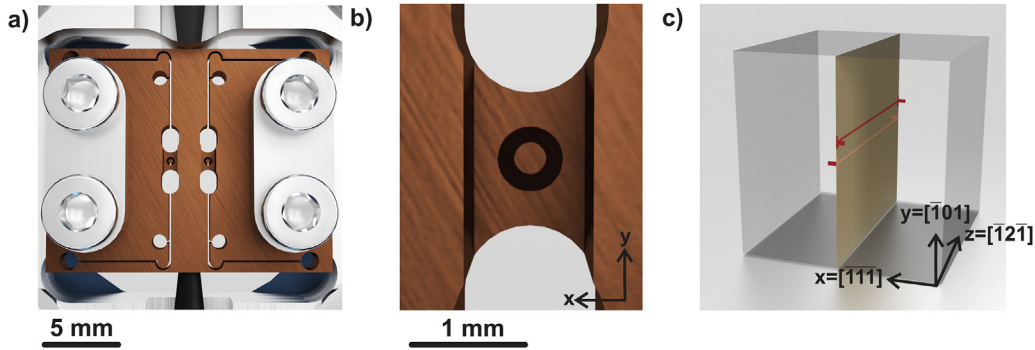


Fig. 2. Detailed information of the geometry of the sample. (a) Schematic view of the sample geometry. The 2 mm thick sample is based on Miyauchi's geometry with two external immobile parts and a central mobile area that can be displaced by two pins. The two symmetric 150 μm thin grooves correspond to the shear zones; (b) Schematic of one of the shear zones. Each shear zone is locally thinned to 30 μm by picosecond pulsed laser ablation with stair-shape in the front side. The inner diameter of the ablated area is 300 μm ; (c) The Cu single crystal is oriented for single slip with its Burgers vector parallel to the shear direction. The axes show the crystallographic orientation.

laser ablation (Fig. 2b) using a commercial picosecond laser (Lumera Laser GmbH, Germany) operated at 355 nm with 50 KHz at 50 mW output power and 10 ps pulse duration. Details on the laser ablation technique can be found in Ref. [31]. The thinning procedure consists of two steps. First, on the front side a circular area with internal diameter of $\sim 300 \mu\text{m}$ is created by gradual stair-shape reduction. Second, on the back side a larger rectangular area is removed resulting in a final thickness of $\sim 30 \mu\text{m}$ within the circular area. This procedure ensures that any damage that may exist at the surface of the original single crystal is removed in the sensitive area where the Laue diffraction measurements are performed. The crystal orientation of the sample is shown in Fig. 2c.

One major consideration for this complex sample geometry is the homogeneity of the applied shear in the central thinned areas. To prove that, crystal plasticity finite element (FEM) simulations [32] were performed using the same geometry and crystal orientation as in the experiments. Constitutive laws based on the phenomenological description of Hutchinson [33] and pure copper single crystal parameters [34–36] were used. Zero displacement boundary conditions were set on the surface between the copper single crystal and the fixing screws. On the central moving area symmetric boundary conditions were imposed. The applied deformation amplitude was 6 μm , which gave a strain of 1.05% at maximum force of 6.62 N. Fig. 3 shows the γ_{xy} strain tensor component at the maximum force in the first cycle. γ_{xy} is the largest strain component and is uniform in the area of interest. Simulations also showed that

$$\gamma \cong \Delta / \varnothing \quad (1)$$

being Δ the displacement of the central moving area (measured by the angular encoder) and \varnothing the inner diameter of the thinned area. The γ_p is later calculated as suggested in Ref. [1].

2.3. Laue diffraction

The Laue diffraction experiments were performed at the MicroXAS beam line of the Swiss Light Source (SLS), located at the Paul Scherrer Institute. Fig. 4 shows the schematic layout of the installed *in situ* setup. A pink x-ray beam with energies ranging between 10 and 23 keV was focused with a pair of Kirkpatrick-Baez (KB) mirrors to a spot size of $700 \times 900 \text{ nm}^2$ as determined by a knife-edge scan. The sample was placed in the focal point, which was located 150 mm downstream from the KB mirrors. The diffracted beam was detected by a DECTRIS EIGER 4M detector with an active area of 2070×2167 pixels and 75 μm pixel size. This state-of-the-art X-ray detector operates in single photon counting mode and provide high dynamic range, zero dark signal and zero readout noise. The sample-to-detector distance was 65 mm, which is equivalent to an angular acceptance of $2\theta = 135^\circ$. The exposure time was 0.3 s. The setup was calibrated with the aid of a 10 μm thin Si wafer. The sample was scanned through the beam along the X and Y direction and at each point a Laue diffraction pattern was recorded. Scans of $10 \times 25 \mu\text{m}^2$ were performed with a step size of 300 nm in the centre of the thinned area.

The Laue diffraction patterns were analysed using in-house

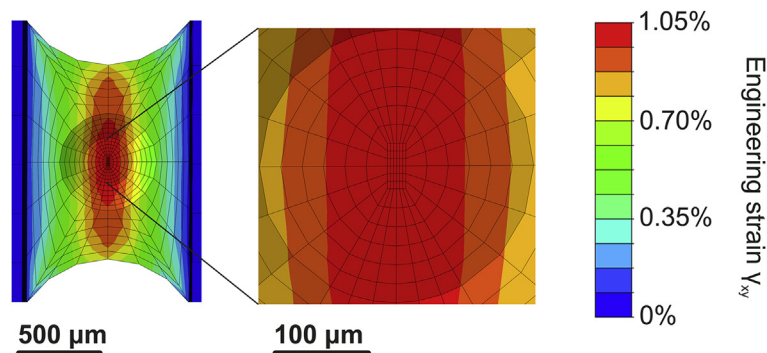


Fig. 3. γ_{xy} distribution for 1.01% strain at maximum force of 6.62 N in the simulated geometry. The area of interest where the Laue scan is performed is zoomed in to check the uniform distribution.

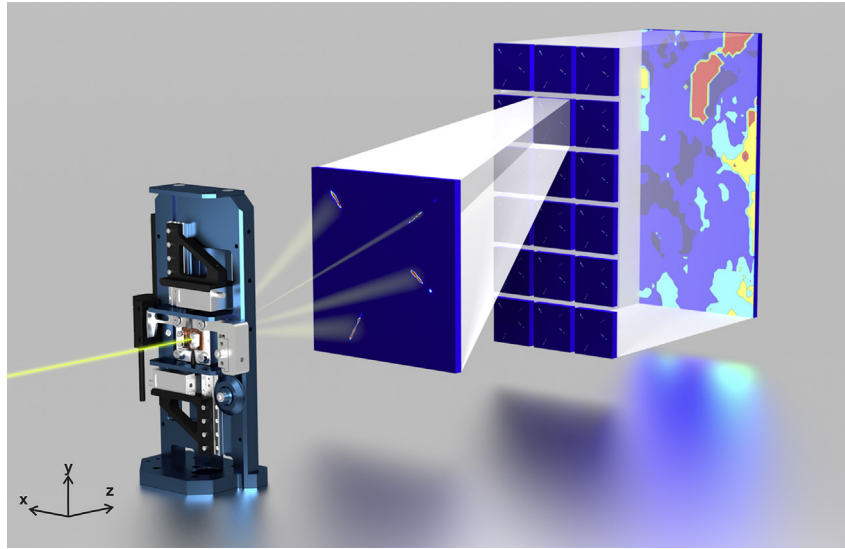


Fig. 4. Schematic layout of the *in situ* X-ray Laue diffraction setup for reversible cyclic shear experiments. Polychromatic x-rays are focused to a spot size of $700 \times 900 \text{ nm}^2$. The sample is mounted in a miniaturized deformation rig, dedicated for reversible shear experiments. The sample is scanned through the beam along the X and Y direction and at each point a Laue diffraction pattern is recorded, providing a spatial resolved misorientation map.

written software. In a first step the Laue diffraction peaks were identified by an automatic indexation routine. Second, the average crystal orientation within the illuminated volume was determined by a refinement procedure yielding an orientation matrix.

The Laue diffraction experiments are performed in transmission geometry. As a consequence, each Laue diffraction spot represents the averaged signal across the sample thickness. Orientation gradients within the gauge volume will result in a spreading of the Laue spots. Statistical information of this spreading can be obtained by a template-matching technique as suggested by Gupta and Agnew [37] and later used by Hofmann et al. [38].

The basic idea is to generate virtual Laue diffraction patterns for various crystal orientations that deviate slightly from the average orientation. For each calculated pattern it is checked whether the calculated diffraction spots all are contained within the experimentally observed diffraction spots. To do that, the experimental peak profiles are binarized by setting the pixel intensity to 0 when the peak intensity is less than 20% of the maximum intensity and to 1 for all other points with higher intensity. In this work, the orientation of the crystal was virtually rocked around its mean position by rotating about the X, Y and Z-axes with a step size of 0.03° such that orientation grid $|\theta_x| = |\theta_y| = |\theta_z| = 1.5^\circ$ is covered. For each matching pattern the crystal orientation is saved, which finally results in a picture of the orientation spread within the gauge volume in terms of three misorientation angles.

2.4. Calculation of misorientation, rotation about X-Y-Z axes and GND density

From the spatial resolved Laue maps misorientation and GND maps are generated. For each point in the map a Bunge orientation matrix G is determined by the above-mentioned refinement routine. A reference matrix is chosen as the point that did not vary its orientation after 120 cycles. For each point in the Laue map, the misorientation and Euler axis compared to the reference orientation (axis-angle representation of a rotation) and the magnitudes of rotation about X, Y and Z axes (ω_x, ω_y and ω_z) are determined.

Disorientation vectors ($\Delta\theta_k$) in sample coordinates are computed as follows:

$$G = (G_A)^{-1} G_B \quad (2)$$

$$\Delta\theta = \arccos((\Delta G_{ii} - 1)/2) \quad (3)$$

$$\Delta\theta_k = -\varepsilon_{kij} \Delta G_{ij} \Delta\theta / 2 \sin \Delta\theta \quad (4)$$

being $k = \{x, y, z\} = \{1, 2, 3\}$ and A and B two neighboring points. Lattice curvatures are then derived as

$$\kappa_{kl} \approx \Delta\theta_k / \Delta L_l \quad (5)$$

with $l = \{x, y\} = \{1, 2\}$, that are then used to calculate the following Nye dislocation density tensor components:

$$\alpha_{12} = \kappa_{21} \quad (6)$$

$$\alpha_{13} = \kappa_{31} \quad (7)$$

$$\alpha_{12} = \kappa_{21} \quad (8)$$

$$\alpha_{21} = \kappa_{12} \quad (9)$$

$$\alpha_{23} = \kappa_{32} \quad (10)$$

$$\alpha_{33} = -\kappa_{11} - \kappa_{22} \quad (11)$$

This procedure has been applied both in EBSD by Pantleon [39] and in three-dimensional X-ray diffraction by Larson et al. [40]. It should be noted that X-ray microdiffraction could underestimate GND densities due to the relatively coarse size and larger beam size comparing to EBSD. The influence of the step size was demonstrated by Wright et al. [41]. Finally an apparent density of GNDs is determined as

$$\rho_{\text{apparent}} = 1/b \cdot (|\alpha_{12}| + |\alpha_{13}| + |\alpha_{21}| + |\alpha_{23}| + |\alpha_{33}|) \quad (12)$$

where b is the Burgers vector [42].

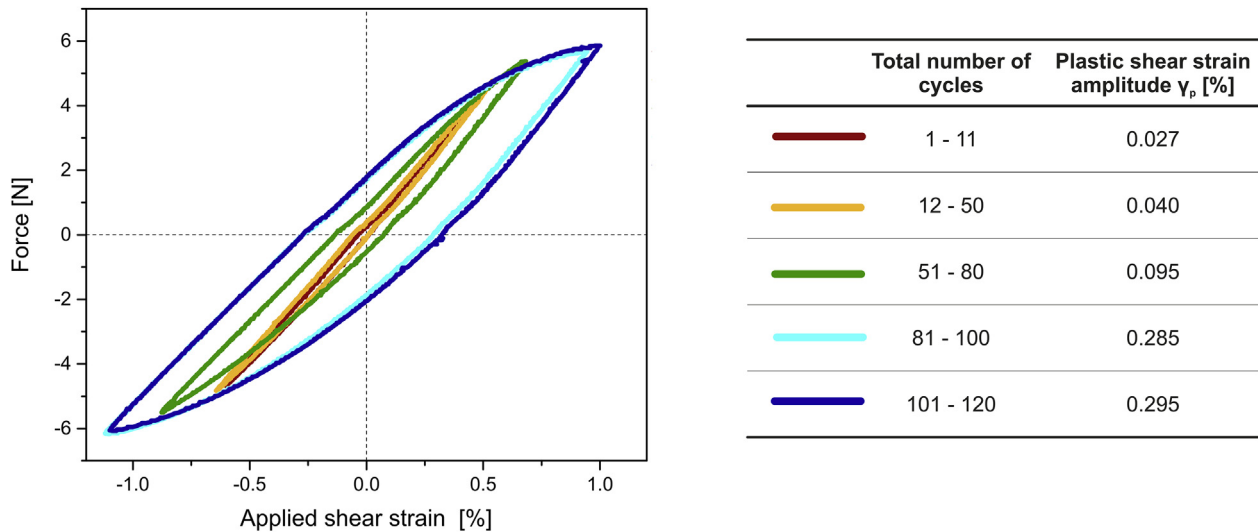


Fig. 5. Mechanical response during reversible cycling. The force response as a function of applied shear strain is shown for the last cycle of each series. The number of cycles and the applied plastic shear strain amplitudes are listed in the table.

3. Results

3.1. Mechanical data

Fully reversible cyclic shear experiments were performed displacement controlled with a fixed displacement rate of 100 nm/s. In total 120 full cycles were completed, subdivided into five series, where the plastic strain amplitude was gradually increased from 0.027% to 0.295%. Fig. 5 displays the corresponding mechanical response evidencing a considerable increase in strain hysteresis after 80 cycles. To resolve the evolution of the local crystallographic orientation spatially resolved Laue diffraction maps were recorded before the first cycle and after 11, 50, 80, 100 and 120 cycles in the unloaded state.

3.2. Evolution of misorientation

Fig. 6a shows the evolution of the scalar misorientation angle as a function of shear cycles within the scanned area. The values are calculated relative to a reference point for which the position of all seven Laue peaks did not change during the 120 cycles. Hence, dark blue areas highlight regions that have the same scalar value of rotation as the reference point.

Before the first shear cycle, a few misoriented regions with dimensions of the order of μm^2 can be distinguished. Region **A** is rotated by 0.15° , region **B** by 0.22° , and regions **C**, **D** and **E** by values less than 0.14° . During the first 80 shear cycles, for which the force-strain hysteresis remains small, the misorientation distribution changes continuously: regions **B** and **D** fragment into smaller regions within the first 11 cycles, region **A** disappears, and region **C** initially increases its rotation till cycle 50 and then decreases it again. Interestingly, after 80 cycles, the scanned region mostly homogenizes to a “background” containing only rotation gradients below 0.05° . Some pre-existing features remain, nevertheless, recognizable, such as the fragmented region **B** and faint footprints of regions **C** and **E**, recognizable by a rotation of 0.13° . Region **D** has reached the same rotation value as it had before cycling.

After an additional 20 cycles at plastic strain amplitude of 0.285%, new rotated areas are appearing. These regions further grow in rotation values and in dimensions during the last 20 cycles at similar shear strain amplitude. Two 0.22° misoriented regions

are formed, one which evolved from the previous fragmented region **B**, and another (marked **F**) from a region that was part of the “background”. These rotated areas are slightly elongated in the $[\bar{1}01]$ slip direction. The scan after 120 cycles evidences other “yellow” regions with increasing scalar misorientation, one which is neighbouring region **D** containing non-mobile dislocations. Close inspection reveals “red” spots that are mobile during cycling up to 120.

3.3. Evolution of rotation about X-Y-Z axes

Fig. 6b–d presents the evolution of the amount of rotation on the X-, Y-, and Z-axes (ω_x, ω_y and ω_z), whose rotation angle limits are $[0.2^\circ]$, $[0.1^\circ]$ and $[0.25^\circ]$, respectively. As in the case of the misorientation map, the initial distribution of the X-Y-Z rotations is not homogeneous. Some domains in the upper part of the ω_x map are rotated positively ($\omega_x \sim 0.04^\circ$ – yellow) and other domains negatively, e.g. the left-bottom corner ($\omega_x < -0.05^\circ$ – dark blue). More locally, one can also find small regions with values of $\omega_x \sim 0.20^\circ$, as is for instance the case in region **C**. The values of ω_y are smaller in magnitude, with some larger regions with an average value of $\omega_y \sim -0.07^\circ$ (dark blue regions). The rotation around the Z axis is most pronounced: positive rotated areas with $\omega_z \sim 0.08^\circ$ (yellow – region **E** and surrounds of region **B**) or $\omega_z \sim 0.22^\circ$ (red – region **B**) can be found. These areas are embedded in a matrix with negative values for $\omega_z \sim -0.6^\circ$ (light blue). The misorientation map and ω_z map show the strongest correlation. In fact, Regions **A** and **B** have predominant rotation about Z-axis, region **E** has a mix about X and Z, and region **C** and **D** are mainly rotated about X and Y respectively.

During the first 80 cycles at low amplitude, the initial X-Y-Z rotation maps are gradually fragmenting as observed for the misorientation maps. The yellow domains in the ω_x maps for example, get smaller. Only region **C** increases its ω_x value. On the other hand, new blue areas appear (left edge) or the initial ones expand. The dark blue-domains of the ω_y map also shrink their size and value. The upper part of the map, on the contrary, tends to rotate to positive ω_y , but the value is never larger than 0.05° . The evolution of ω_z during cycling is very similar as what was observed for the misorientation map: the pronounced fragmentation of regions **B** and **E**, followed by a re-building of a larger misoriented region in **E**.

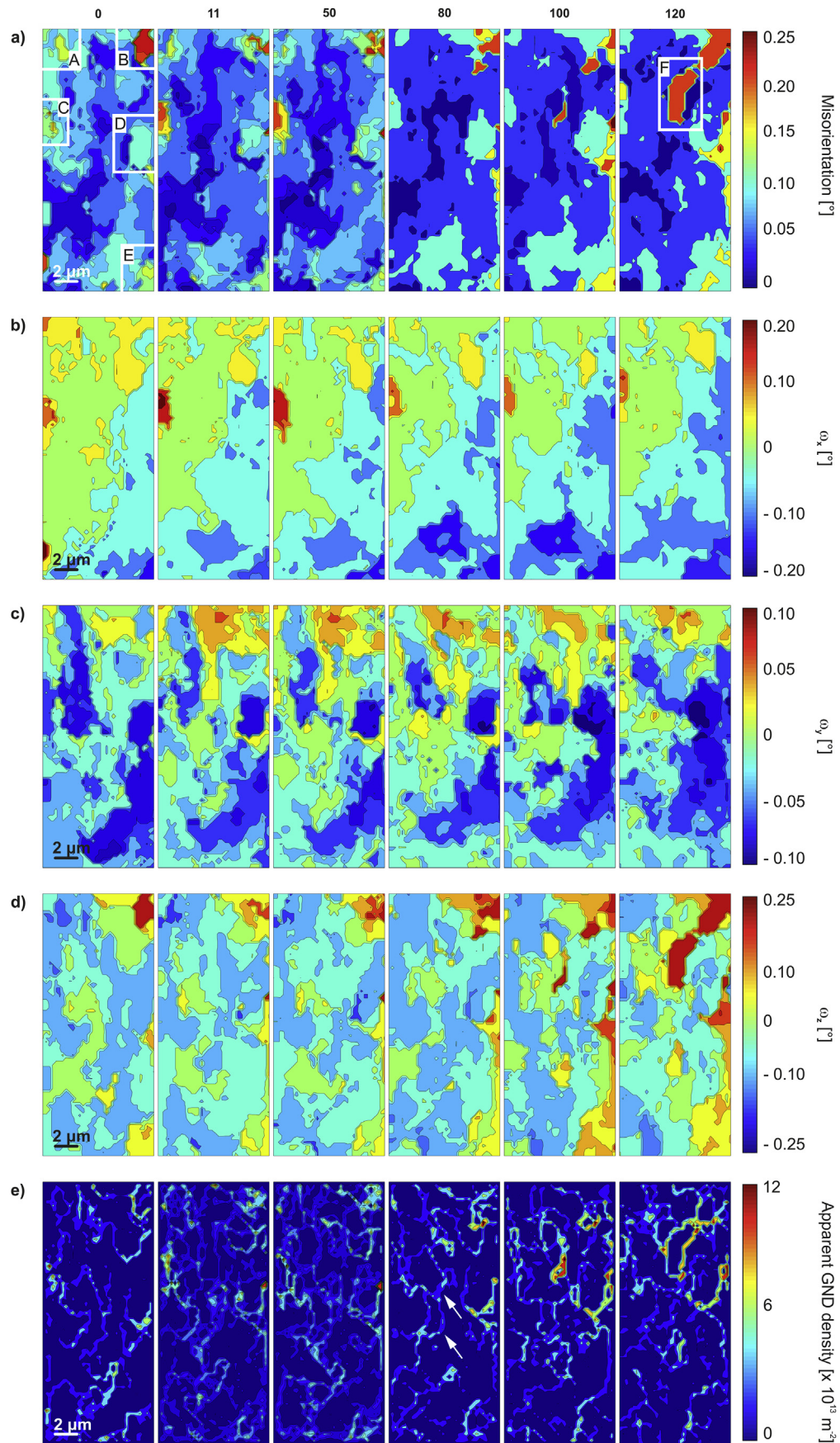


Fig. 6. Evolution of local misorientation, rotation about X-, Y-, Z-axes and apparent density of geometrically necessary dislocations during reversible cycling integrated over the sample thickness. (a) Spatial resolved maps of local misorientation at various stages of cycling. Six regions of interest (label A – F) are marked by white boxes; (c–d) Evolution of the rotations on the X-, Y-, and Z-axes (ω_x, ω_y and ω_z); (e) Evolution of the apparent GND density.

During the last 40 cycles (from 80 to 120), ω_z maps are the ones experiencing most of the changes. The regions with high misorientation value also have the higher positive rotation about Z-axis (regions **B** and **F** and the surrounds of **D**). In the ω_y maps at 120 cycles, two defined globes with $\omega_y \sim -0.7^\circ$ are appreciable. One corresponds to the initial region **D** and lies between two highly $+\omega_z$ rotated regions (region **F** and the surround of **D**); the other one is located below region **D** and neighbours the highly $+\omega_z$ rotated region. No special changes are notorious in the ω_x maps.

3.4. Evolution of GND densities

The apparent GND density evolution is displayed in Fig. 6e. Already in the as-prepared state several tracks with non-zero GND density can be observed. Most of them mark partially the perimeter of rotated regions, others however cross regions that have similar misorientation angle. The latter means that among regions with similar rotation angle, there are sub-regions with different Euler axis.

During the first 50 cycles, the GND density distribution exhibits a dynamical behaviour; in some areas the GND density decreases whereas in others it increases. New faint traces appear as consequence of the reorganization observed in the misorientation map and $\omega_x, \omega_y, \omega_z$ rotation maps (step 11 and 50). After a total of 80 cycles, the GND map shows again clear GND traces that overlap almost entirely the boundaries of the misoriented regions. The correlation is however stronger with the ω_z map. For instance, in the right side to region **C**, there are several closed circuits of GND traces (pointed with white arrows) that do not have direct connection with the misorientation map but are associated to low misoriented regions observable in ω_z .

At cycle 100, a new cluster with a GND density of $10 \times 10^{13} \text{ m}^{-2}$ is observed corresponding with the onset of region **F**. At cycle 120,

region **F** has grown into a homogeneous rotated region surrounded by high density GND boundaries. Also Region **D** is separated by a GND wall from the newly growing rotated area underneath.

3.5. Evolution of peak shape

Fig. 7 shows a zoom-in of the misorientation map around the highest rotated area at 0, 80, 100 and 120 cycles (region **F** in Fig. 6a). Two positions are indicated for which the evolution of the (400) diffraction peak is shown, being the most sensitive reflection to the primary dislocations in this single slip orientation. Initially, the peak profile is narrow as expected for a single crystal. In position 1 the volume over which the signal is integrated progressively splits in sub-regions. After 120 cycles the volume has largely rotated over 0.23° . On the contrary, the peak profile in position 2 first only slightly changes its intensity distribution during homogenization and then stays unaffected by the last shear cycles. Note that for both positions, all other high intensity diffraction peaks have initial similar profiles as (400), but remain mostly unaffected by the cycling. This confirms that during shear cycle, only one type of slip system is activated.

To get statistical information on the orientation spread in the beam direction the template matching technique is applied in Position 1 and Position 2 at cycle 0 and cycle 120. Fig. 8 shows the misorientation spread in the scattering volume, where the small rotation angles around X, Y and Z-axes (θ_x , θ_y and θ_z) are given in degrees. It is important to note that the amount of points within a certain orientation region is not proportional to the volume of that region. The colour of each point (presented by the scale bar) corresponds to the normalized intensity of the (400) reflection shown in Fig. 7. The orientation spread prior to cycling is very similar for positions 1 (Fig. 8a) and 2 (Fig. 8b), which can be ascribed to the initial defect content due to the sample preparation. After 120

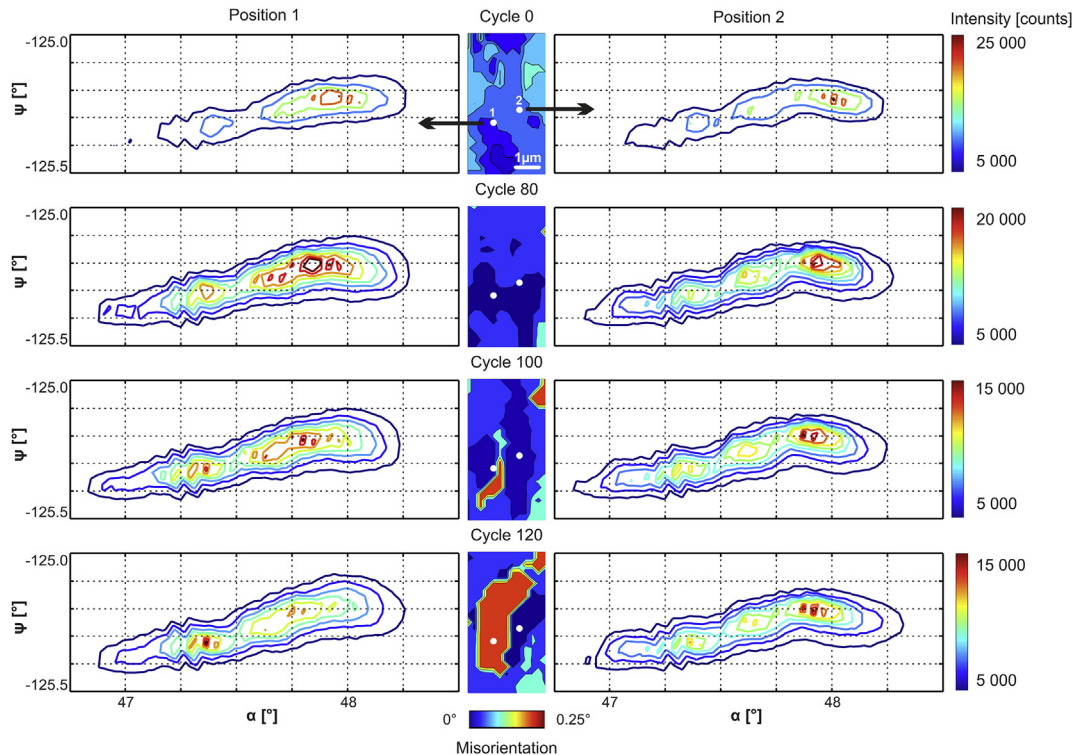


Fig. 7. Evolution of the (400) diffraction peak during reversible cycling. Contour plots of the (400) diffraction peak at two positions in region **F** (as marked in Fig. 6a) at 4 different stages of cycling. α denotes the angle between the incoming and the diffracted beam (radial) and Ψ is the azimuthal angle on the detector plane.

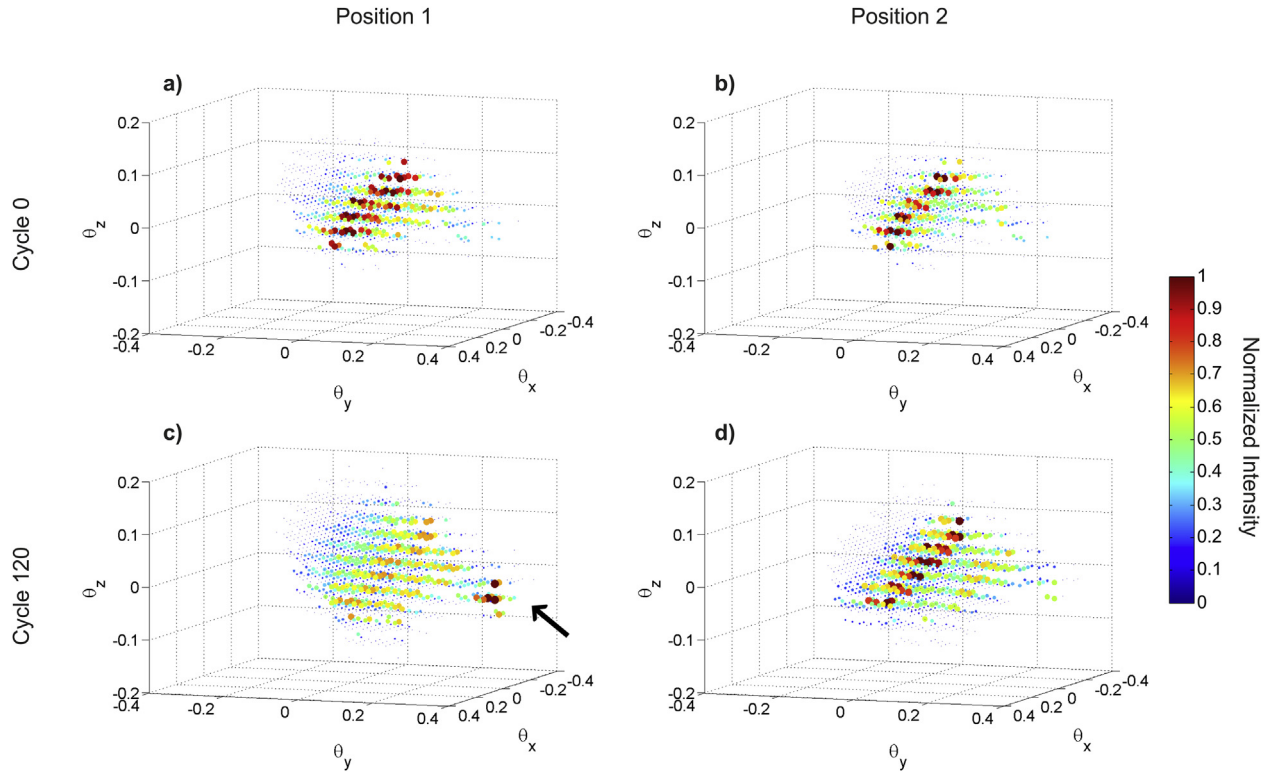


Fig. 8. Misorientation spread in the integrated volume of Positions 1 and 2 in the initial (a and b) and final stage (c and d). θ_x , θ_y and θ_z are small rotations around X, Y and Z-axes.

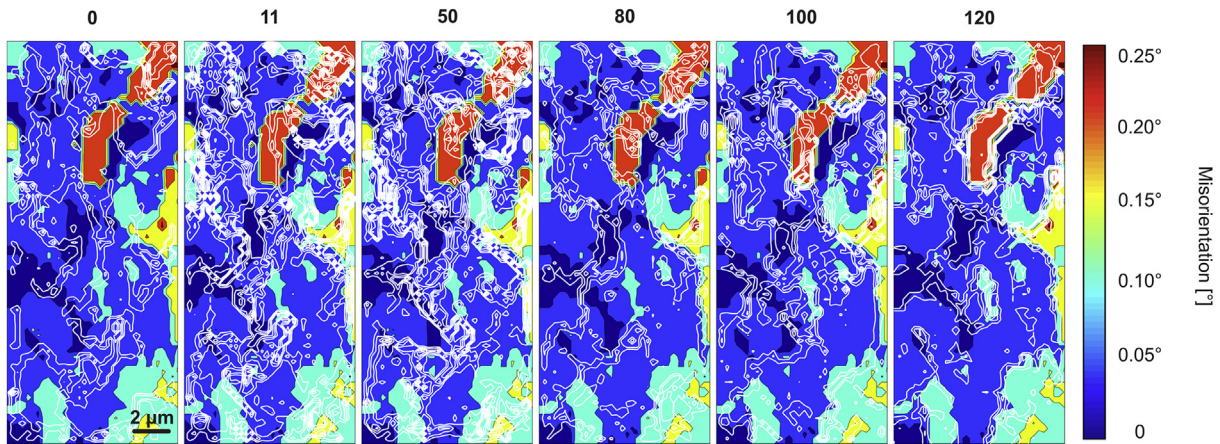


Fig. 9. Evolution of the GND density traces at cycles 0, 11, 50, 80, 100 and 120 on top of the misorientation map after 120 cycles.

cycles the positions of the points with maximum intensity for the cloud of position 1 are shifted (Fig. 8c) and a new misoriented region is formed as indicated in Fig. 8 by the black arrow. This evidences the formation of a volume with different orientation and whose orientation spread is less than that of the initial microstructure. Traces of the initial microstructure are still observable suggesting that the new region did not yet grow over the entire 30 microns over which the signal is integrated. On the other hand, the points with maximum intensity for the cloud corresponding to position 2 (Fig. 8d) remain at similar positions.

4. Discussion

The developed miniaturized shear device together with the

chosen sample geometry in the above performed experiment allows following the evolution of rotations during cyclic shear in a volume of $10 \times 25 \times 30 \mu\text{m}^3$. The sample has initially a certain dislocation density due to the sample preparation technique applied. Because the Cu single crystal is oriented for single slip with its Burgers vector parallel to the shear direction, only a part of the pre-existing dislocations are mobile. The observed homogenization process during the initial loading cycles at low amplitudes, accompanied with a continuous change in local misorientation, points to a certain mobility of the dislocation network. The remaining traces of initial misorientation after 80 cycles have to be ascribed to pre-existing non-mobile dislocations. Careful inspection shows that the GND traces observed at cycle 0 are not dominating the formation of GNDs that define region F after 120 cycles.

Fig. 9 shows the GND traces (in white) at cycles 0, 11, 50, 80 100 and 120 on top of the misorientation map after 120 cycles, where rotated region **F** is clearly defined. As it can be observed, the physical location of the initial GND traces does not match with region **F**. This is different for region **B** where the rotated area after 120 cycles is clearly related to the presence of pre-existing immobile dislocations. The evolution of the GND traces shows a clear redistribution of the pre-existing GNDs, the appearance of new GNDs that are responsible for the evolving rotated regions. The location of these regions can be determined by pre-existing dislocations or simply evolving from accumulation of new GNDs such as region **F**, which after 120 cycles is clearly defined by a surrounding GND trace. Thus, the presence of the initial mobile/immobile dislocations plays a role in the microstructural evolution as they can act as pinning points or dislocation sources and participate in the development of dislocation ensembles.

The expected dislocation structure due to the applied shear fatigue consists of accumulation of edge dipoles on the primary (111) slip plane with Burgers vectors $\bar{1}01$. This arrangement causes rotation about an axis parallel to the $[1\bar{2}1]$ direction. In Fig. 6d it can be observed that the major rotation of region **F** is in fact about the Z axis $[1\bar{2}1]$. Still, the alignment of dislocation ensembles in other regions is expected to evolve during more cycles and to continue till saturation stage, as it was reported by others [5,43]. The amount of misorientation is also in good agreement with the range of values reported by other authors for cyclically deformed fcc specimens [44,45]. Moreover, the fact that region **F** does not contain internally GNDs but is surrounded by a GND wall supports the description of accumulation of edge dipoles, since the latter do not contribute to curvature [46].

As a consequence, the observed dynamics evidences the formation of a vein in region **F**, surrounded by a channel and the above analysis presents for the first time a cartoon of dislocation patterning during cyclic deformation with quantitative information on lattice curvature and GND densities. During the initial cycles in this single slip oriented shear experiment, strain hysteresis remains small and mobile dislocations are swept around homogenizing the microstructure. The presence of non-mobile dislocations is marked by local tracks with low GND densities. The formation of the first heterogeneous structures characterized by the presence of GND walls and the formation of newly rotated regions are marked by an increasing strain hysteresis. Regions with higher rotations grow by accumulation of GNDs generated during cycling. Edge dipoles accumulate first loosely, and then confined while increasing the misorientation of the growing vein structure. Surrounding areas stay depleted from dislocations. The position of a rotated area can be related to pre-existing non-mobile dislocation structures as is the case for region **B**.

It is important to bear in mind that the method here developed is a quasi 2D approach, since the GND densities are integrated over the thickness of the sample. This excludes the study of many multi-slip deformation geometries during which 3D cell structures are formed [11]. For that purpose, the 3D x-ray microscopy method permits measuring three-dimensionally the local lattice rotations with micron resolution in the third dimension. The data collection is however extremely time consuming and therefore excludes *in situ* measurements after cyclic loading steps or under load during continuous deformation.

The approach we propose sacrifices on the fully 3D aspect but it brings the time resolved aspects and the spatially resolved GND density evolution required during deformation. Interestingly, it is applied on a sample volume that is very similar what advanced modelling methods can now simulate. The error made by integration will depend on the design of the deformation experiment i.e. the character of the GND network expected. Our approach is one

step further towards synergies with computational models. For instance our method can be used to validate three-dimensional discrete dislocation models or density based dislocation dynamics models (e.g. Refs. [9,13,15]) when applied in deformation geometries where the formation of 2D dislocation patterns is expected such as for instance dislocation accumulation in veins, walls, persistent slip bands or oligocrystals.

5. Conclusion

In conclusion, using micro-beam x-ray Laue diffraction we have provided the first quantitative information on the transition from uniform to non-uniform dislocation structures in a Cu crystal during cyclic shear. The proposed method is fast, allows imaging of areas far beyond typical pattern dimensions and provides information on rotational gradients and GND densities over several tens of microns, i.e. lengthscales similar to those addressable in dislocation density based computational models [13,47]. It can be applied synergistically for validating predictions of dislocation patterning up to large deformation strains during continuous loading or to study the formation of persistent slip bands after many more fatigue. It therefore has a large potential to facilitate a breakthrough in our understanding of 2D dislocation patterning and our possibilities to predict failure by advancing computational models. The proposed technique is complementary to 3D x-ray microscopy using wire techniques [22] and 3D-EBSD [21], both restricted to a snapshot in time of the microstructure. Together they have the potential to boost synergies between modelling and experiment.

Acknowledgements

A.I.-L., H.V.S., N.G. and S.V.P. thank the Swiss National Science Foundation for financial support (SNF – 138240). H.V.S. thanks the European Research Council for the advanced grant MULTIAx (339245). The authors thank Dr. A. Guitton and Dr. R. Broennimann for the help in sample preparation; B. Meyer and M. Birri for beamline support; Dr. J. Gaudenz, S. Ebner, Dr.T. Celcer for the help in the integration of the detector; M. Dzambegovic for graphical support and S. Zhen and S. Zabihzadeh for beamtime support.

References

- [1] S. Suresh, *Fatigue of Materials*, Cambridge University Press, 1998.
- [2] A. Argon, *Strengthening Mechanisms in Crystal Plasticity*, Oxford University Press, 2007.
- [3] L.E. Levine, B.C. Larson, W. Yang, M.E. Kassner, J.Z. Tischler, M.A. Delos-Reyes, et al., X-ray microbeam measurements of individual dislocation cell elastic strains in deformed single-crystal copper, *Nat. Mater.* 5 (2006) 619–622, <http://dx.doi.org/10.1038/nmat1698>.
- [4] B. Jakobsen, H.F. Poulsen, U. Lienert, J. Almer, S.D. Shastri, H.O. Sørensen, et al., Formation and subdivision of deformation structures during plastic deformation, *Science* 312 (2006) 889–892, <http://dx.doi.org/10.1126/science.1124141>.
- [5] H. Mughrabi, Deformation-induced long-range internal stresses and lattice plane misorientations and the role of geometrically necessary dislocations, *Philos. Mag.* 86 (2006) 4037–4054, <http://dx.doi.org/10.1080/14786430500509054>.
- [6] P. Li, S.X. Li, Z.G. Wang, Z.F. Zhang, Fundamental factors on formation mechanism of dislocation arrangements in cyclically deformed fcc single crystals, *Prog. Mater. Sci.* 56 (2011) 328–377, <http://dx.doi.org/10.1016/j.pmatsci.2010.12.001>.
- [7] R. LeSar, Simulations of dislocation structure and response, *Annu. Rev. Condens. Matter Phys.* 5 (2014) 375–407, <http://dx.doi.org/10.1146/annurev-conmatphys-031113-133858>.
- [8] L. Kubin, *Dislocations, Mesoscale Simulations and Plastic Flow*, Oxford University Press, 2013.
- [9] A.M. Hussein, S.I. Rao, M.D. Uchic, D.M. Dimiduk, J.A. El-Awady, Microstructurally based cross-slip mechanisms and their effects on dislocation microstructure evolution in fcc crystals, *Acta Mater.* 85 (2015) 180–190, <http://dx.doi.org/10.1016/j.actamat.2014.10.067>.

- [10] R. Madec, B. Devincere, L. Kubin, Simulation of dislocation patterns in multislip, *Scr. Mater.* 47 (2002) 689–695, [http://dx.doi.org/10.1016/S1359-6462\(02\)00185-9](http://dx.doi.org/10.1016/S1359-6462(02)00185-9).
- [11] S. Xia, A. El-Azab, Computational modelling of mesoscale dislocation patterning and plastic deformation of single crystals, *Model. Simul. Mater. Sci. Eng.* 23 (2015) 055009, <http://dx.doi.org/10.1088/0965-0393/23/5/055009>.
- [12] T. Hochrainer, S. Sandfeld, M. Zaiser, P. Gumbsch, Continuum dislocation dynamics: towards a physical theory of crystal plasticity, *J. Mech. Phys. Solids* 63 (2014) 167–178, <http://dx.doi.org/10.1016/j.jmps.2013.09.012>.
- [13] S. Sandfeld, M. Zaiser, Pattern formation in a minimal model of continuum dislocation plasticity, *Model. Simul. Mater. Sci. Eng.* 23 (2015) 065005, <http://dx.doi.org/10.1088/0965-0393/23/6/065005>.
- [14] N. Grilli, K.G.F. Janssens, H. Van Swyghoven, Crystal plasticity finite element modelling of low cycle fatigue in fcc metals, *J. Mech. Phys. Solids* 84 (2015) 424–435, <http://dx.doi.org/10.1016/j.jmps.2015.08.007>.
- [15] G. Po, M.S. Mohamed, T. Crosby, C. Erel, A. El-Azab, N. Ghoniem, Recent progress in discrete dislocation dynamics and its applications to micro plasticity, *JOM* 66 (2014) 2108–2120, <http://dx.doi.org/10.1007/s11837-014-1153-2>.
- [16] M.F. Ashby, The deformation of plastically non-homogeneous materials, *Philos. Mag.* 21 (1970) 399–424, <http://dx.doi.org/10.1080/14786437008238426>.
- [17] J.F. Nye, Some geometrical relations in dislocated crystals, *Acta Metall.* 1 (1953) 153–162, [http://dx.doi.org/10.1016/0001-6160\(53\)90054-6](http://dx.doi.org/10.1016/0001-6160(53)90054-6).
- [18] A. Needleman, J.G. Sevillano, Preface to the viewpoint set on: geometrically necessary dislocations and size dependent plasticity, *Scr. Mater.* 48 (2003) 109–111, [http://dx.doi.org/10.1016/S1359-6462\(02\)00336-6](http://dx.doi.org/10.1016/S1359-6462(02)00336-6).
- [19] J. Ahmed, S.G. Roberts, A.J. Wilkinson, Characterizing dislocation structure evolution during cyclic deformation using electron channelling contrast imaging, *Philos. Mag.* 86 (2006) 4965–4981, <http://dx.doi.org/10.1080/14786430600710941>.
- [20] A.J. Wilkinson, T.B. Britton, J. Jiang, P.S. Karamched, A review of advances and challenges in EBSD strain mapping, *IOP Conf. Ser. Mater. Sci. Eng.* 55 (2014) 012020, <http://dx.doi.org/10.1088/1757-899X/55/1/012020>.
- [21] E. Demir, D. Raabe, N. Zaafarani, S. Zaefferer, Investigation of the indentation size effect through the measurement of the geometrically necessary dislocations beneath small indents of different depths using EBSD tomography, *Acta Mater.* 57 (2009) 559–569, <http://dx.doi.org/10.1016/j.actamat.2008.09.039>.
- [22] B.C. Larson, W. Yang, G.E. Ice, J.D. Budai, J.Z. Tischler, Three-dimensional X-ray structural microscopy with submicrometre resolution, *Nature* 415 (2002) 887–890, <http://dx.doi.org/10.1038/415887a>.
- [23] F. Hofmann, B. Abbey, W. Liu, R. Xu, B.F. Usher, E. Balaur, et al., X-ray micro-beam characterization of lattice rotations and distortions due to an individual dislocation, *Nat. Commun.* 4 (2013), <http://dx.doi.org/10.1038/ncomms3774>.
- [24] Rozaliya I. Barabash, Gene E. Ice, Diffraction analysis of defects: state of the art, in: *Strain Dislocation Gradients Diffr*, Imperial College Press, 2014, pp. 1–52.
- [25] M.S. Mohamed, B.C. Larson, J.Z. Tischler, A. El-Azab, A statistical analysis of the elastic distortion and dislocation density fields in deformed crystals, *J. Mech. Phys. Solids* 82 (2015) 32–47, <http://dx.doi.org/10.1016/j.jmps.2015.05.011>.
- [26] L.E. Levine, C. Okoro, R. Xu, Full elastic strain and stress tensor measurements from individual dislocation cells in copper through-Si vias, *IUCr* 2 (2015) 635–642, <http://dx.doi.org/10.1107/S2052252515015031>.
- [27] J.W.L. Pang, W. Liu, J.D. Budai, G.E. Ice, Inhomogeneous deformation behavior in intercrystalline regions in polycrystalline Ni, *Acta Mater.* 65 (2014) 393–399, <http://dx.doi.org/10.1016/j.actamat.2013.11.008>.
- [28] F. Ackermann, L.P. Kubin, J. Lepinoux, H. Mughrabi, The dependence of dislocation microstructure on plastic strain amplitude in cyclically strained copper single crystals, *Acta Metall.* 32 (1984) 715–725, [http://dx.doi.org/10.1016/0001-6160\(84\)90145-7](http://dx.doi.org/10.1016/0001-6160(84)90145-7).
- [29] Z.S. Basinski, S.J. Basinski, Fundamental aspects of low amplitude cyclic deformation in face-centred cubic crystals, *Prog. Mater. Sci.* 36 (1992) 89–148, [http://dx.doi.org/10.1016/0079-6425\(92\)90006-S](http://dx.doi.org/10.1016/0079-6425(92)90006-S).
- [30] K. Miyauchi, A proposal of a planar simple shear test in sheet metals, *Sci. Pap. Inst. Phys. Chem. Res.* 78 (1984) 27–40.
- [31] A. Guitton, A. Irastorza-Landa, R. Broennimann, D. Grolimund, S. Van Petegem, H. Van Swyghoven, Picosecond pulsed laser for microscale sample preparation, *Mater. Lett.* 160 (2015) 589–591, <http://dx.doi.org/10.1016/j.matlet.2015.06.119>.
- [32] F. Roters, P. Eisenlohr, L. Hantcherli, D.D. Tjahjanto, T.R. Bieler, D. Raabe, Overview of constitutive laws, kinematics, homogenization and multiscale methods in crystal plasticity finite-element modeling: theory, experiments, applications, *Acta Mater.* 58 (2010) 1152–1211, <http://dx.doi.org/10.1016/j.actamat.2009.10.058>.
- [33] J.W. Hutchinson, Bounds and self-consistent estimates for creep of polycrystalline materials, *Proc. R. Soc. Math. Phys. Eng. Sci.* 348 (1976) 101–127, <http://dx.doi.org/10.1098/rspa.1976.0027>.
- [34] O. Dmitrieva, P.W. Dondl, S. Müller, D. Raabe, Lamination microstructure in shear deformed copper single crystals, *Acta Mater.* 57 (2009) 3439–3449, <http://dx.doi.org/10.1016/j.actamat.2009.03.035>.
- [35] C. Déprés, M. Fivel, L. Tabourot, A dislocation-based model for low-amplitude fatigue behaviour of face-centred cubic single crystals, *Scr. Mater.* 58 (2008) 1086–1089, <http://dx.doi.org/10.1016/j.scriptamat.2008.02.027>.
- [36] W.C. Overton, J. Gaffney, Temperature variation of the elastic constants of cubic elements. I. Copper, *Phys. Rev.* 98 (1955) 969–977, <http://dx.doi.org/10.1103/PhysRev.98.969>.
- [37] V.K. Gupta, S.R. Agnew, Indexation and misorientation analysis of low-quality Laue diffraction patterns, *J. Appl. Crystallogr.* 42 (2009) 116–124, <http://dx.doi.org/10.1107/S0021889808042349>.
- [38] F. Hofmann, X. Song, B. Abbey, T.-S. Jun, A.M. Korsunsky, High-energy transmission Laue micro-beam X-ray diffraction: a probe for intra-granular lattice orientation and elastic strain in thicker samples, *J. Synchrotron Radiat.* 19 (2012) 307–318, <http://dx.doi.org/10.1107/S0909049512003044>.
- [39] W. Pantleon, Resolving the geometrically necessary dislocation content by conventional electron backscattering diffraction, *Scr. Mater.* 58 (2008) 994–997, <http://dx.doi.org/10.1016/j.scriptamat.2008.01.050>.
- [40] B.C. Larson, J.Z. Tischler, A. El-Azab, W. Liu, Dislocation density tensor characterization of deformation using 3D X-ray microscopy, *J. Eng. Mater. Technol.* 130 (2008) 021024, <http://dx.doi.org/10.1115/1.2884336>.
- [41] S.I. Wright, D.P. Field, M.M. Nowell, Post processing effects on GND calculations from EBSD-based orientation measurements, *IOP Conf. Ser. Mater. Sci. Eng.* 89 (2015) 012049, <http://dx.doi.org/10.1088/1757-899X/89/1/012049>.
- [42] V.K. Gupta, S.R. Agnew, A simple algorithm to eliminate ambiguities in EBSD orientation map visualization and analyses: application to fatigue crack-tips/wakes in aluminum alloys, *Microsc. Microanal.* 16 (2010) 831–841, <http://dx.doi.org/10.1017/S1431927610093992>.
- [43] J. Yang, Y. Li, C. Ma, G. Li, Simulation and observation of dislocation pattern evolution in the early stages of fatigue in a copper single crystal, *Mater. Sci. Eng. A* 299 (2001) 51–58, [http://dx.doi.org/10.1016/S0921-5093\(00\)01415-5](http://dx.doi.org/10.1016/S0921-5093(00)01415-5).
- [44] M. Wilkens, K. Herz, H. Mughrabi, An X-ray diffraction study of cyclically and of unidirectionally deformed copper single crystals, *Z. Für Met.* 71 (1980) 376–386.
- [45] H. Mughrabi, Dual role of deformation-induced geometrically necessary dislocations with respect to lattice plane misorientations and/or long-range internal stresses, *Acta Mater.* 54 (2006) 3417–3427, <http://dx.doi.org/10.1016/j.actamat.2006.03.047>.
- [46] A. Arsenlis, D. Parks, Crystallographic aspects of geometrically-necessary and statistically-stored dislocation density, *Acta Mater.* 47 (1999) 1597–1611, [http://dx.doi.org/10.1016/S1359-6454\(99\)00020-8](http://dx.doi.org/10.1016/S1359-6454(99)00020-8).
- [47] J.W. Kysar, Y. Saito, M.S. Oztop, D. Lee, W.T. Huh, Experimental lower bounds on geometrically necessary dislocation density, *Int. J. Plast.* 26 (2010) 1097–1123, <http://dx.doi.org/10.1016/j.ijplas.2010.03.009>.